A Finite Element Model of the Foot/Ankle to Evaluate Injury Risk in Various Postures

CHRIS SMOLEN[1] and CHERYL E. QUENNEVILLE[1,2]

[1]Department of Mechanical Engineering, McMaster University, 1280 Main Street West, Hamilton, ON L8S 4L7, Canada; and [2]School of Biomedical Engineering, McMaster University, Hamilton, ON, Canada

Associate Editor Joel D. Stitzel oversaw the review of this article.

Abstract—The foot/ankle complex is frequently injured in many types of debilitating events, such as car crashes. Numerical models used to assess injury risk are typically minimally validated and do not account for ankle posture variations that frequently occur during these events. The purpose of this study was to evaluate a finite element model of the foot and ankle accounting for these positional changes. A model was constructed from computed tomography scans of a male cadaveric lower leg and was evaluated by comparing simulated bone positions and strain responses to experimental results at five postures in which fractures are commonly reported. The bone positions showed agreement typically within 6° or less in all anatomical directions, and strain matching was consistent with the range of errors observed in similar studies (typically within 50% of the average strains). Fracture thresholds and locations in each posture were also estimated to be similar to those reported in the literature (ranging from 6.3 kN in the neutral posture to 3.9 kN in combined eversion and external rotation). The least vulnerable posture was neutral, and all other postures had lower fracture thresholds, indicating that examination of the fracture threshold of the lower limb in the neutral posture alone may be an underestimation. This work presents an important step forward in the modeling of lower limb injury risk in altered ankle postures. Potential clinical applications of the model include the development of postural guidelines to minimize injury, as well as the evaluation of new protective systems.

Keywords—Strain, Hindfoot, Kinematics, Load, Lower limb, Ankle, Posture, Fracture.

INTRODUCTION

The ankle is the most common site of injury for occupants during frontal vehicular collisions[34] and over 150,000 Americans suffer from moderate-to-untreatable lower limb injuries every year due to this injury mechanism alone.[42] Improvised explosive device (IED) detonations in combat zones[38] and falls from a height also frequently cause damage to this area. Due to poor vascularity, ankle injuries often result in long-term impairment,[39] resulting in excessive healthcare costs,[30] inability to work,[6] and chronic emotional distress.[39]

By understanding the factors that cause ankle injury, suitable protective systems can be designed, reducing these negative outcomes. The reusability, realism and relatively low cost of finite element (FE) models makes them a valuable tool in the automotive and defense industries to evaluate injury in a wide variety of loading conditions,[43] and for use in the development of protective devices. Advantages of FE simulations over tests using current industry-standard anthropomorphic test devices (ATDs) include greater geometric and material biofidelity, lower cost, and the ability to obtain model outputs, such as strain, at any location.[9]

Several dynamic injury-predicting lower leg and ankle models have been constructed,[45,53] but are usually based on scaled[24] or simplified[10] geometry, with relatively coarse meshes (>3 mm average element size). Many ligaments are often missing that play a role in load transfer between bones and control relative bone positions.[1,10,24] Finally, complex bone geometry often leads to elements with high degrees of distortion, and potentially poor model accuracy,[56] yet most studies do not report element quality.

Model validation has historically been limited, and is usually accomplished by comparing the overall force–time response of the model at the proximal tibia with biofidelity corridors (mean curves ± 1 SD)

generated from cadaveric specimens in analogous experimental tests.[24] This verifies that the "global" model response falls within the range expected in the human population, but does not ensure accurate behavior of individual model components, such as specific bones. Accurate behavior of individual model components is important for accurate failure location and load prediction, since these component interactions are the basis for the failure mechanisms of the lower leg and ankle.[48] When assessing the behavior of bones (by investigating the strain field, for instance), finer meshes than those implemented in previous studies would be necessary to accurately model localized bone responses.

Furthermore, validation is typically performed with the ankle in a neutral posture,[1,10,24] and while the model response may be accurate for this one posture, there is no guarantee that the same will be true for other postures the ankle may assume. Accounting for variation in ankle posture is important for injury prediction, as this may alter the fracture threshold and location throughout this region.[27] Recently, a few studies have attempted to evaluate the responses of lower limb FE models at various ankle postures.[44,45] In these studies, the sole of the foot was rigidly fixed to the footplate and ankle posture was altered by rotating the footplate. Due to the complex nature of simulating bone-to-bone contact in FE models, the ankle bone positions that resulted from this footplate rotation may not necessarily be true to the actual positions these bones would adopt in the natural ankle, and no investigations were performed to verify whether this is the case. Furthermore, model evaluation continued to consist of overall global force–time or moment–angle responses.

The objectives of this study were three-fold: first, to construct an FE model of the lower limb and ankle with higher quality bone meshes than those seen in previous studies from CT scans of a cadaveric specimen, including 67 ligaments. Second, to evaluate the response of this model at the component level at five ankle postures previously demonstrated to be particularly vulnerable to injury, based on the positions and rotations of the bones and the strains on the bone surfaces. Third, to predict the fracture load and location in all ankle postures in pure compression.

METHODS

Model Construction

The experimental study is described in a previous paper,[49] but is summarized here briefly. Six strain gauge rosettes (I274-UFRA-1-23-3L, Hoskin Scientific Ltd., Burlington, ON, Canada) were attached to the ankle bones of a fresh-frozen male cadaveric left lower leg (age 46, sectioned at the tibial plateau, with no history of leg or ankle injury or surgery) at the tibia (1), fibula (2), medial calcaneus (3), lateral calcaneus (4), medial talar neck (5) and talar sulcus (6) (Fig. 1). The proximal end of the leg was potted and attached to a CT-compatible device capable of adjusting the angle of the ankle independently in three dimensions *via* a footplate while applying static axial loads up to 667 N (150 lbs). First, a Computed Tomography (CT) scan (Philips Brilliance Big Bore, 120 kV, 249.48 mA, 1 mm axial slice thickness, 0.32 mm in-plane resolution) of the leg was taken in the neutral posture with no load applied. Neutral posture was defined as having the plantar aspect of the foot completely on the transverse plane, perpendicular to the shank, with a line drawn from the back of the heel to the space between the first and second toes aligned to the sagittal plane. Next, CT scans of the leg were acquired and strains were simultaneously recorded in response to static axial loads of 667 N (150 lbs) in five postures: neutral, 18° of inversion with 10° of external rotation, 18° of eversion with 10° of external rotation, 22° of plantarflexion, and 13° of dorsiflexion with 18° of inversion. The weight of 667 N was chosen as it is around the safe upper load limit for a weight suspended from the end of the CT scanner bed. Coordinate systems were developed for each bone of the hindfoot[49] (tibia, fibula, talus and calcaneus), and the Euler angles of the talus and calcaneus in the adjusted postures were calculated relative to the neutral posture. In the neutral posture, Euler angles were calculated relative to the unloaded case. The experimental Euler angles of the hindfoot bones in each posture were calculated so that they could be compared to those calculated from the rotations of the bones of the FE lower limb described in this study, determining whether attaching the plantar surface of a lower limb FE model to a footplate, and rotating the footplate to induce ankle rotation results in accurate ankle bone positions.

The CT scan from the neutral, unloaded posture was imported into Mimics® (Materialise, Leuven, Belgium), and the tibia, fibula, calcaneus and talus were separated into cortical and cancellous regions based on Hounsfield Unit thresholding (cortical: 226-3071 HU, cancellous < 226 HU). The bones of the hindfoot were the focus of the model since they are the primary load path through this region[21] and the most debilitating ankle injuries are experienced by these bones.[31] The geometry of the remaining 24 midfoot/forefoot bones and the plantar soft tissues were not segmented into cancellous and cortical bone regions, and were instead each defined by an overall "bone" thresholding. All bones and the plantar soft tissues were separate entities and none were rigidly connected to one another. 3D surfaces were generated from the regions

defined during thresholding, and the Cartesian coordinates of the six strain gauges were identified.

Ankle bone and plantar soft tissue meshes were generated using TrueGrid (XYZ Scientific Inc., Livermore, CA, USA). The meshes were projected onto the 3D surfaces, and were manipulated until acceptable element quality was achieved, defined as avoiding elements with Jacobians less than 0.25, interior angle deviations greater than 70° and aspect ratios less than 10, as these were the mesh quality goals most commonly cited in previous studies describing the creation of biomechanical FE models with hexahedral meshes.[3,37,54] All regions were meshed with hexahedral elements, except the thin cortical talus and calcaneus, which were represented by quadrilateral shells. Shell thicknesses were determined based on a distance map generated between the cortical and cancellous surfaces using Mimics®, and were found to be relatively uniform except at the exceptionally thin lateral calcaneus (Fig. 2). The midfoot/forefoot bones were meshed automatically (using Mimics®) with tetrahedral elements and assigned rigid properties.

The meshes were imported into LS-Dyna® (LSTC, Livermore, CA, USA), and contact was defined between bones with the coefficient of friction of articular cartilage (0.02) assigned.[36] The elements at the six strain gauge locations were identified based on their positions in the CT scans.

Sixty-seven ligaments were included as 1-D bar elements, the insertion sites of which were determined based on ligamentous dissections of the foot and ankle documented in anatomical textbooks, journal papers and illustrations.[18,19,41] These sites were identified independently by four investigators, and their positions averaged to minimize potential bias.

The tibial and fibular ligaments were assigned nonlinear force–displacement equations,[14] while the tibionavicular ligament was assigned a linear stiffness.[47] Material properties of midfoot ligaments and hindfoot ligaments connecting the talus and calcaneus were assumed to be the same as those for the anteriortalofibular ligament scaled by the ratio between their respective cross-sectional areas.[45] Forefoot ligaments were assigned linear stiffnesses,[8,20,26,28,50] and where material properties were unavailable, were assumed to have the same properties as the dorsal intermetatarsal ligament[45] (Tables 1, 2, and 3).
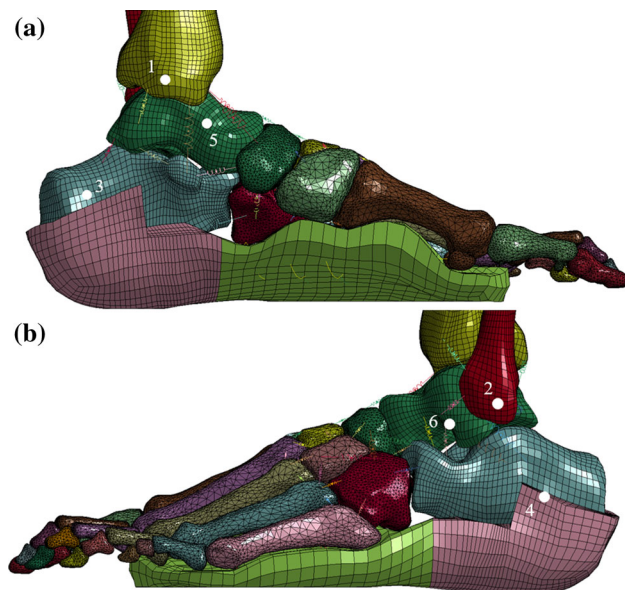

FIGURE 1. Strain gauge locations. The locations of the six strain gauges attached to the bones of the lower leg and are indicated by white dots on the medial (a) and lateral (b) views of the FE model. The gauges were located on the apex of the medial malleolus of the tibia (1), the apex of the lateral malleolus of the fibula (2), the medial calcaneus, midway between the posterior-most bugle of calcaneal tuberosity and the apex of the posterior articular surface for the talus (3), the lateral calcaneus, midway between the posterior-most bulge of the calcaneal tuberosity and the fibular trochlea (4), the medial talar neck, immediately superior to the articulating surface for the plantar calcaneonavicular ligament (5) and the apex of the opening to the talar sulcus (6).
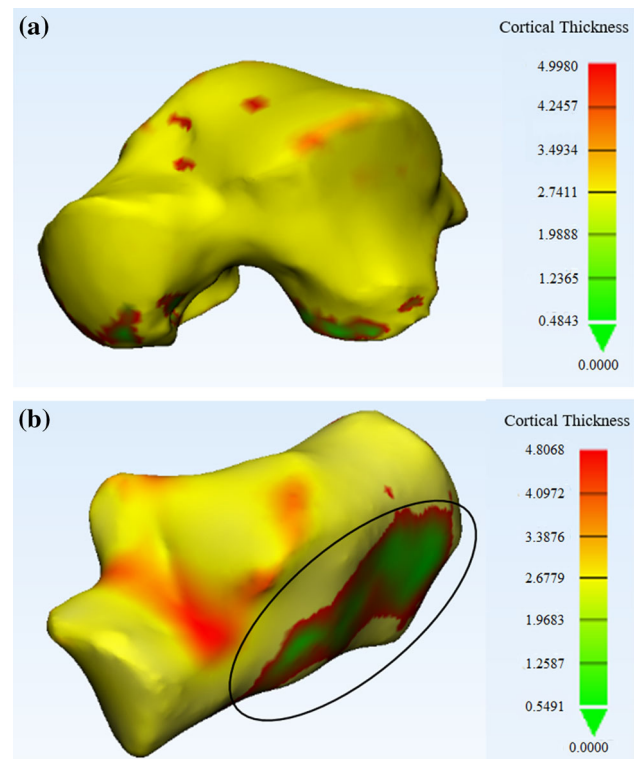

FIGURE 2. Talus and calcaneus shell thicknesses. A distance map was generated between the cortical and cancellous regions of the talus (a) and calcaneus (b) (scale in mm). A relatively consistent thickness was observed of around 2.74 mm for the talus and 2.68 mm for the calcaneus. The lateral calcaneus had a thinner cortical shell, at an average of 1.25 mm (indicated by the black oval).

Boundary Conditions

The experimental boundary conditions were simulated by meshing a footplate positioned underneath the plantar soft tissues, and by fixing the proximal end of the shank in all degrees of translation and rotation to simulate the pot. The rotation axes of the ankle about the three anatomical directions (plantar/dorsiflexion, inversion/eversion, external/internal rotation) were determined by identifying lines connecting two consistent points per rotation direction in the CT scans of the different postures. The center of rotation between the neutral and repositioned postures was found by determining the intersection of the perpendicular bisectors of each of these lines before and after rotation from the CT scans. Each of the experimentally-tested postures was simulated in the model by rigidly attaching the plantar surface of the foot to the footplate, and moving the footplate into its final position as determined from these centers of rotation (Fig. 3). The explicit solver in LS-Dyna was used for all simulations. All rotations were performed over a relatively long timeframe of 200 ms to minimize any dynamic effects. An axial load increasing linearly from 0 to 667 N (150 lbs) was then applied through the footplate over 125 ms, followed by a constant force held for 25 ms, ensuring quasi-static strain rates in the bones (<0.01 s^{-1}),[46] which was verified in the model. These loading rates were in line with the slow loading that was applied experimentally.

Model Calibration and Material Properties

The plantar soft tissue material was assigned an Ogden rubber material (MAT_77), and the peak plantar soft tissue compression was measured at the metatarsal heads and calcaneus from the neutral posture CT scans under load. Three simulations were performed in which the material parameters (μ,α) of this region were altered within the normal physiological range of plantar soft tissue stiffness provided in a study by Erdemir et al.[11] ($\mu = 16.45$ kPa and $\alpha = 6.82$; $\mu = 20.59$ kPa and $\alpha = 7.61$; $\mu = 24.72$ kPa and $\alpha = 8.39$; corresponding to 50, 75 and 100% of max physiological stiffness) until the aggregate error between the experimental and simulated compression for this sweep of material parameters was minimized.

All bones were defined as elastic–plastic (MAT_24), and the cortical and cancellous tibia and fibula were assigned the properties from a study by Quenneville and Dunning[37] (cortical modulus: 17 GPa, cancellous modulus: 0.4 GPa). Using the optimal plantar soft tissue properties (as determined above), the calcaneus and talus bone properties were altered over 30 simulations until the total summed error was minimized between experimental and simulated strain values at the gauge locations. Different modulus assignments for different bones is common for lower limb FE models,[10,24] and therefore each hindfoot bone (and bone type) was optimized independently.

For the talus, a parametric study was performed in which different combinations of cortical and cancellous moduli were assigned within the natural range[1,25,40,44] until the error between simulated and experimental strains at the gauge locations was minimized (cortical = 12, 14, 17, 20, 22.5 GPa, cancellous = 0.25, 0.32, 0.4 GPa). The same procedure was then repeated for the calcaneus, except for the extremely thin lateral cortical portion of this bone, which was assigned a relatively low cortical modulus of 12 GPa[1] to increase simulation strains in this region. Due to their highly inhomogeneous microstructures,[57] different regions within the talus and calcaneus exhibit variations in moduli.

Model Evaluation

For each posture at the maximum load, the Euler angles and displacements of the calcaneus and talus bones were calculated in the same manner as during experimental testing.[49] The angles and displacements

TABLE 1. Tibia, fibula and forefoot ligament properties.

Ligament	a (N)	b
Anterior talofibular	7.18	12.50
Anterior tibiofibular	5.52	22.63
Anterior tibiotalar	2.06	20.11
Calcaneofibular	0.20	49.63
Posterior talofibular	0.14	44.35
Posterior tibiofibular	6.87	20.07
Posterior tibiotalar	1.34	28.65
Tibiocalcaneal	0.51	45.99
Tibionavicular	$k = 39.1$ N/mm	

Ligament properties for eight ligaments that connect the tibia and fibula with the bones of the foot and ankle are expressed as curve fit data (a and b) for an elastic force–strain response function[14] ($T(\varepsilon) = a(e^{b\varepsilon} - 1)$). The stiffness k of the tibionavicular ligament is also provided.[47]

TABLE 2. Calcaneus, talus and midfoot bone ligament properties.

Ligament	Area (mm^2)	Area ratio	References
Anterior talocalcaneal	14.4	0.229	23
Posterior talocalcaneal	14.96	0.238	32
Lateral talocalcaneal	6.84	0.109	32
Medial talocalcaneal	14.91	0.237	32
Interosseous talocalcaneal	72.80	1.158	23
Dorsal talonavicular	35.15	0.559	32
Interosseous calcaneocuboid	72.80	1.158	23
Plantar calcaneocuboid	98.70	1.570	45
Calcaneonavicular	9.23	0.147	32
Plantar calcaneonavicular	161.00	2.560	33
Dorsal cuboideonavicular	13.10	0.208	32
Plantar cuboideonavicular	27.80	0.442	45
Interosseous cuboideonavicular	14.01	0.223	32
Plantar cuneonavicular (Med)	12.59	0.200	32
Plantar Cuneonavicular (Int)	8.10	0.129	32
Plantar cuneonavicular (Lat)	7.12	0.113	32
Dorsal cuneonavicular 1 (Med)	6.46	0.103	32
Dorsal cuneonavicular 2 (Int)	10.33	0.164	32
Dorsal cuneonavicular 3 (Lat)	11.61	0.185	32
Dorsal cuneocuboid	7.52	0.120	32
Plantar cuneocuboid	13.80	0.219	32
Dorsal intercuneiform (Lat to Int)	13.80	0.220	45
Dorsal intercuneiform (Int to Med)	13.80	0.220	45
Plantar intercuneiform (Lat to Int)	13.80	0.220	45
Plantar intercuneiform (Int to Med)	13.80	0.220	45
Interosseous intercuneiform (Lat to Int)	121.07	1.925	33
Interosseous intercuneiform (Int to Med)	121.07	1.925	33

Properties for the calcaneal, talar and midfoot bone ligaments were assumed to be the same as the anterior-talofibular ligament, scaled by their relative cross-sectional areas. The anterior-talofibular ligament has a cross-sectional area of 62.85 mm[33] and areas for all other ligaments were provided by Imhauser,[23] Mkandawire[32,33] and Shin.[45] For ligaments involving the cuneiform bones, Lat, Int and Med refer to the lateral, intermediate and medial cuneiforms, respectively.

were calculated using anatomical landmarks, with the x-axis pointed approximately in the superior direction, the y-axis in the anterior direction, and the z-axis in the lateral direction. Surface strains from the elements at the strain gauge locations were also acquired from the simulations, and were averaged over the last 10 ms of the simulation to represent the steady state level.

Repeated trials were not performed during experimental testing in the various postures due to time limitations, and so two times the neutral trial average standard deviation (90 $\mu\varepsilon$) was selected to be the acceptable difference between strains in the simulation and experiment. The average neutral standard deviations of the Euler angles and displacements were extremely small (1.2° and 1.3 mm), and so more reasonable differences of 6° and 3 mm between the simulation and experiment were selected as the threshold of being acceptable. These limits are on the order of the standard deviations of strain and bone rotation relative to the mean that were observed within the population in previous studies,[2,47,52] suggesting that these limits constitute a critical evaluation of the model.

A Bland–Altman plot was created using the strain values from each gauge (location) in all postures to investigate the possibility of systemic errors. Finally, to evaluate the mesh density, the neutral posture model was remeshed by using the mesh splitting function within LS-PrePost, whereby every hexahedral element in the model was divided in half in each direction, generating eight smaller brick elements. The locations of the strain gauges were identified on the new model, and output strains compared between the fine and coarse meshes.

Failure Prediction

The maximum simulated strains in each bone were measured, and the force that would cause fracture in each posture was predicted based on a linear extrapolation of the force–strain response up to the critical strain thresholds for cortical and cancellous bone reported in the literature (0.016 and 0.134, respectively).[5,29] Due to point-loading effects, ligament con-

TABLE 3.   Forefoot ligament properties.

Ligament	Insertion points	Stiffness k (N/mm)	References
Dorsal tarsometatarsal	Meta1/Med cuneiform	115.0	50
	Meta2/Med cuneiform	115.0	50
	Meta2/Int cuneiform	115.0	50
	Meta2/Lat cuneiform	115.0	50
	Meta3/Lat cuneiform	115.0	50
	Meta4/Lat cuneiform	115.0	50
	Meta4/cuboid	115.0	50
	Meta5/cuboid	115.0	50
Plantar tarsometatarsal	Meta1/Med cuneiform	90.0	50
	Meta2/Med cuneiform	90.0	50
	Meta3/Med cuneiform	90.0	50
	Meta4/cuboid	90.0	50
	Meta5/cuboid	90.0	50
Interosseous tarsometatarsal	Meta2/Med cuneiform	189.7	28
	Meta2/Lat cuneiform	189.7	28
	Meta3/Lat cuneiform	189.7	28
Dorsal intermetatarsal	Meta1/Meta2	125.0	20
	Meta2/Meta3	125.0	20
	Meta3/Meta4	125.0	20
	Meta4/Meta5	125.0	20
Plantar	Meta1/Meta2	125.0	20
Intermetatarsal	Meta2/Meta3	125.0	20
	Meta3/Meta4	125.0	20
	Meta4/Meta5	125.0	20
Plantar fascia	Meta1/calcaneus	203.3	26
	Meta2/calcaneus	203.3	26
	Meta3/calcaneus	203.3	26
	Meta4/calcaneus	203.3	26
	Meta5/calcaneus	203.3	26
Long plantar ligament		75.9	8

Linear elastic stiffness values reported in the literature for the forefoot ligaments are provided.[20,26,28,50] Since many ligaments share the same name in this part of the foot, the insertion points of each ligament are given, with Meta referring to a metatarsal, and Med, Int and Lat referring to medial, intermediate and lateral for the cuneiforms.

nection nodes and elements immediately adjacent to them were excluded from these evaluations.

RESULTS

The meshes were composed of 450,580 hexahedral and 3954 shell elements (tibia: 380,400 hex; fibula: 13,024 hex; talus: 20,000 hex, 1640 shell; calcaneus: 30,618 hex, 2314 shell; plantar tissue: 6538 hex). Element Jacobians ranged from 0.17 to 10.4 with a mean of 1.8. Only 10 elements (0.002%) were below the defined threshold, and all were located at the diaphysis–epiphysis transition region in the fibula. The interior element angle deviations from 90° ranged from −79.5° to 84.2° with a mean of 0°. While a few elements in each mesh exceeded the established threshold, the overall number was small (0.04% of all elements), and these elements were not at critical locations. Element aspect ratios ranged from 1.0 to 36.4, but hindfoot and plantar soft tissue (focus of this study) aspect ratios were all less than 10. The tibia and fibula had several elements exceeding this threshold in the center of the diaphyseal regions due to dramatic changes in cortical thickness over their lengths. The overall percentage of elements exceeding this threshold (2.4%) was still minimal, and observed to not be at an area of great interest.

The stiffest plantar soft tissue properties minimized the total summed error in tissue compression (100% stiffness). The total summed error in talar strains was minimized by applying cortical and cancellous moduli of 12 and 0.25 GPa, respectively, while for the calcaneus, this was with cortical and cancellous moduli of 22.5 and 0.32 GPa, respectively (Fig. 4). All assigned bone and plantar soft tissue properties are provided (Table 4).

The Euler angles and displacements of the talus and calcaneus between the simulations and the analogous experiments[49] demonstrated good agreement (Euler angles < 6°, displacements < 3 mm) in all five postures (Fig. 5) except for calcaneal displacement in eversion–
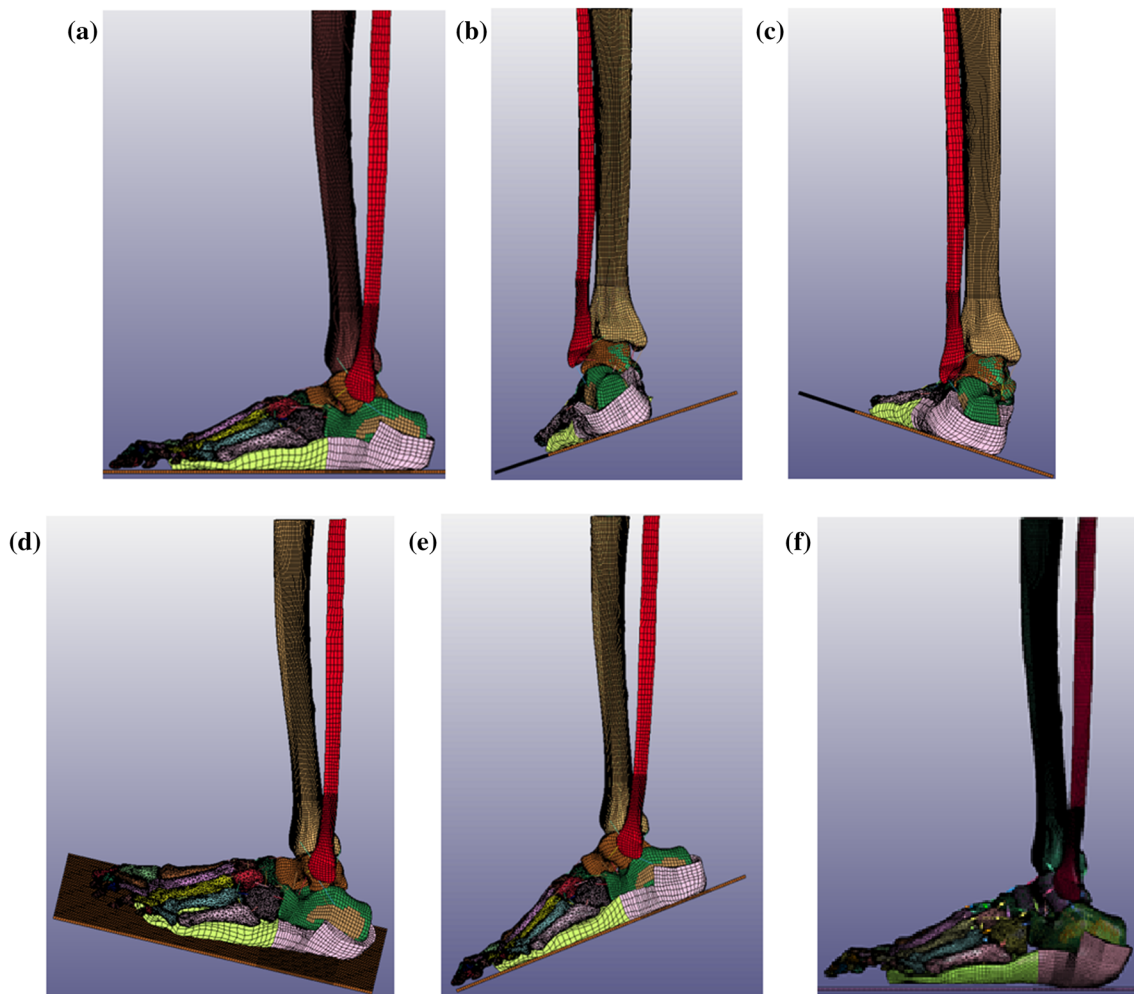
FIGURE 3. The complete lower leg FE model in the five ankle postures. The ankle is shown in the five ankle postures that were tested: neutral (a), 18° of inversion with 10° of external rotation (b), 18° of eversion with 10° of external rotation (c), 13° of dorsiflexion with 18° of inversion (d) and 22° of plantarflexion (e), as well as the refined mesh that was created for the neutral posture (f). These postures resulted from attaching the footplate to the plantar surface of the FE model foot and rotating the footplate by the specified angles about the centers of rotation determined experimentally from the CT scans.

external rotation, which was overestimated in the simulation by 5.5 mm.

The simulated surface strains and those acquired from the analogous experimental results[49] in all five postures were plotted (Fig. 6). Tibial strains had an acceptable level of agreement (<90 $\mu\varepsilon$) for all postures. Fibular strains had acceptable agreement for three of the postures, but were underestimated by the simulation for the neutral and plantarflexion cases. Calcaneal strains had acceptable agreement for both gauges in eversion–external rotation and plantarflexion, and also agreed for one gauge in all other postures. For the talus, agreement was achieved for the gauge attached to the talar sulcus in eversion–external rotation and plantarflexion. The Bland–Altman plot from all strain data in all postures (excluding the medial talar gauge during plantarflexion) showed

minimal bias offset but large 95% limits of agreement (Fig. 7).

The refined (fine) mesh consisted of 3,620,456 elements in the deformable parts (vs. 454,534 in the coarse mesh) (Fig. 3f). Increasing the number of elements also increased the run time by approximately 30-fold. The maximum and minimum principal strains showed good agreement between the models, with the strains overall in the fine mesh being an average of 3% lower than those of the coarse model.

All bones exhibited the highest fracture load (lowest fracture risk) in the neutral posture, while the lowest fracture load (highest fracture risk) was 3.90 kN at the talus in eversion–external rotation (the tibia had a fracture load of 3.92 kN in the same posture) (Fig. 8). The tibial plafond was always the most vulnerable location for the shank. For the neutral and plan-

tarflexion postures, the maximum talar and calcaneal strains were located centrally at the talar sulcus and the posterior articular surface for the talus, respectively. In the postures involving inversion, maximum hindfoot
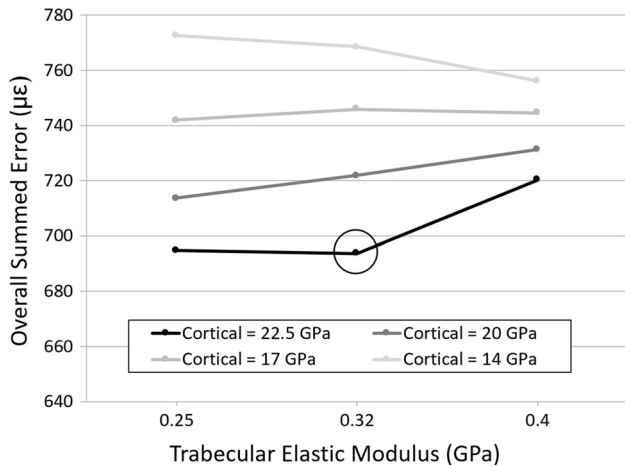

FIGURE 4. Net error in neutral posture strains for selection of calcaneal modulus values. The overall summed error in strains between the experiment and simulation in the neutral posture are provided for twelve different combinations of calcaneal cortical and cancellous bone elastic modulus. The cortical moduli were set to 14, 17, 20 and 22.5 GPa, while the cancellous moduli were set to 0.25, 0.32 and 0.4 GPa. The total error was summed from the individual errors at the six strain gauge locations. The circle indicates the bone properties (cortical = 22.5 GPa, trabecular = 0.32 GPa) that minimized the error between the simulation and experiment.

strains were located medially, around the sustentaculum, while eversion caused these strains to be located laterally, at the angle of Gissane. Maximum strain contour plots for the talus, calcaneus and shank in the neutral posture, the calcaneus in inversion–external rotation, and the talus in eversion–external rotation provide an overall picture of the strain field in the hindfoot in the neutral posture, as well as the strain fields in the calcaneus and talus for the two positions in which these bones are at the greatest risk of injury (Fig. 9).

In the neutral, eversion–external rotation and plantarflexion postures, the talus was at the greatest fracture risk, while for positions involving inversion, the shank was at the greatest fracture risk. The inversion–external rotation posture caused the greatest vulnerability to fracture in the calcaneus.

DISCUSSION

This study presents the only known investigation of the accuracy of bone positions and strains in response to ankle posture adjustment and load application in an FE model of the foot and ankle. The model geometry was developed from CT scans of the cadaveric leg upon which experimental testing was performed, allowing for direct comparison of bone rotations, positions and strains between the simulation and experiment at five vulnerable postures. This also

TABLE 4. Bone and soft plantar tissue properties.

Region	Material parameter	Parameter value	Reference
Cortical bone	Tibia/fibula E	17 GPa	37
MAT_24	Talus E	12 GPa	Current Study Model Calibration
Elastic–plastic	Calcaneus E	22.5 GPa	Current Study Model Calibration
	Lateral calcaneus E	12 GPa	1
	σ_y	0.125 GPa	5
	E_{tan}	1 GPa	5
	ρ	1850 kg m^{-3}	37
	v	0.3	54
Cancellous bone	Tibia/fibula E	0.4 GPa	37
MAT_24	Talus E	0.25 GPa	Current Study Model Calibration
Elastic–plastic	Calcaneus E	0.32 GPa	Current Study Model Calibration
	σ_y	0.01 GPa	25
	E_{tan}	5% of E	22
	ρ	1000 kg m^{-3}	37
	v	0.3	54
Marrow	E	0.2 GPa	7
MAT_1	ρ	1000 kg m^{-3}	7
Elastic	v	0.35	7
Plantar soft tissue	μ	24.72 kPa	11
MAT_77	α	8.39	11
Ogden Rubber	ρ	1000 kg m^{-3}	17
	v	0.49	17

The material model and corresponding properties applied to each bone and the soft plantar tissues are provided. All bone adhered to an elastic–plastic material model with an elastic modulus (E), yield strength (σ_y), plastic "tangent" modulus (E_{tan}), density (ρ) and Poisson's ratio (v). The tibia also included a linear elastic marrow region with an elastic modulus (E), density (ρ) and Poisson's ratio (v). The plantar soft tissues adhered to a hyperelastic Ogden rubber model with material parameters μ and α, density (ρ) and Poisson's ratio (v).

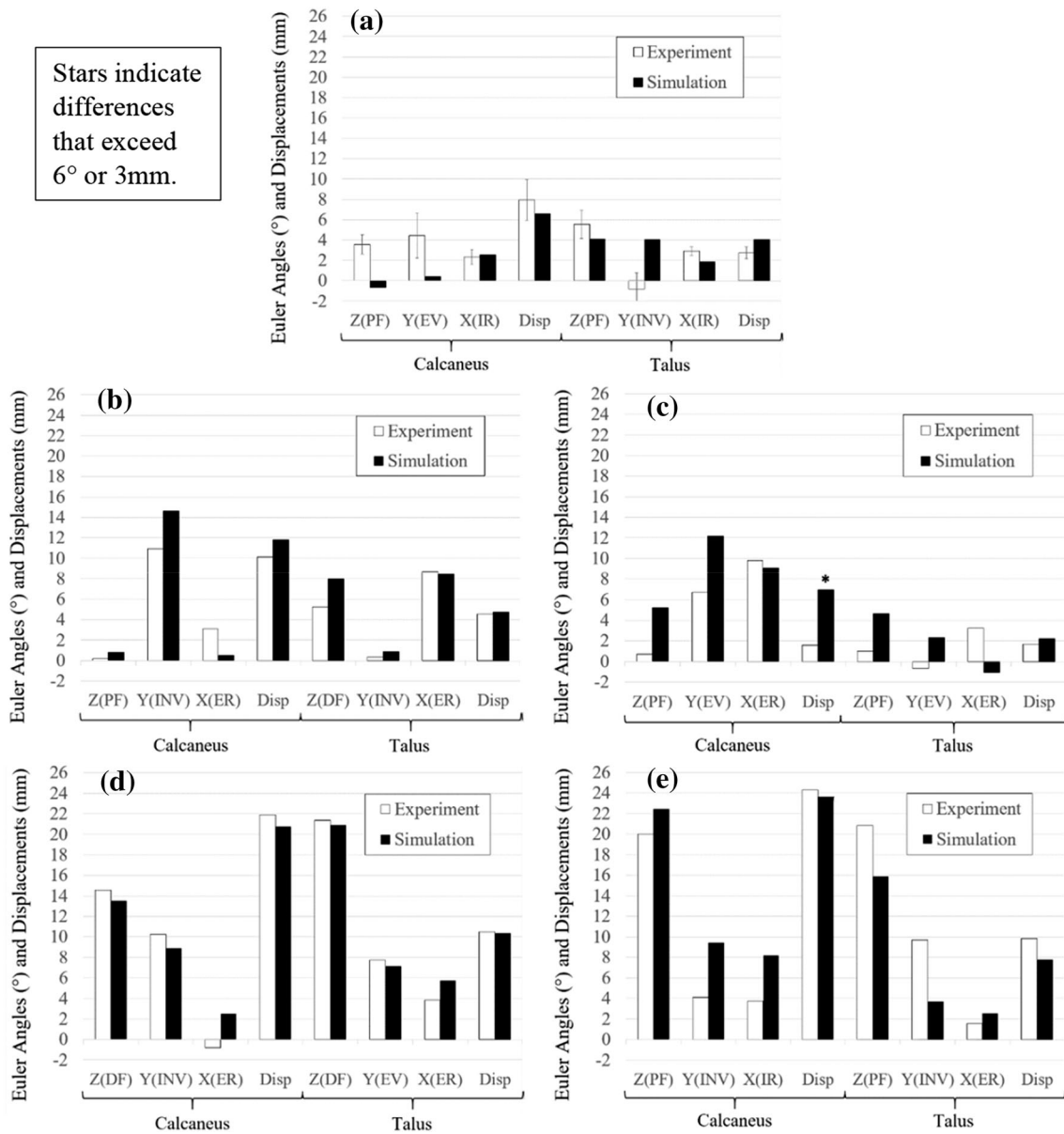Stars indicate differences that exceed 6° or 3mm.

FIGURE 5. Comparison of experimental and simulated Euler angles and displacements. In the neutral (a), inversion–external rotation (b), eversion–external rotation (c), dorsiflexion-inversion (d) and plantarflexion (e) postures, the Euler angles and displacements of the chosen origins of the talus and calcaneus are provided for the FE simulation and the analogous experiment.[49] Z, Y and X represent the Euler angle rotations about the dorsiflexion (DF)/plantarflexion (PF), inversion (INV)/eversion (EV), and internal rotation (IR)/external rotation (ER) axes, respectively. ''Disp'' is the displacement of the origin, which is located at the calcaneal notch and talar posterior tubercle for the calcaneus and talus, respectively. Stars indicate differences that exceed 6° or 3 mm.

allowed the model properties to be tuned to the experimental response. While most lower limb FE models are evaluated globally against biofidelity corridors from previously-published whole bone response data in the neutral posture,[1,24] this study provides the first evaluation of the model response at the component level of the individual ankle bones in a variety of postures.

The FE model is one of the more complex constructed to date, comprising 28 geometrically accurate bones connected by 67 ligaments, 35 of which were assigned non-linear force–displacement relationships. The bone meshes were very fine relative to those seen in previous studies,[10] with the largest hindfoot bone surface element size in this study (3 mm) corresponding to the smallest seen previously. Furthermore, spe-
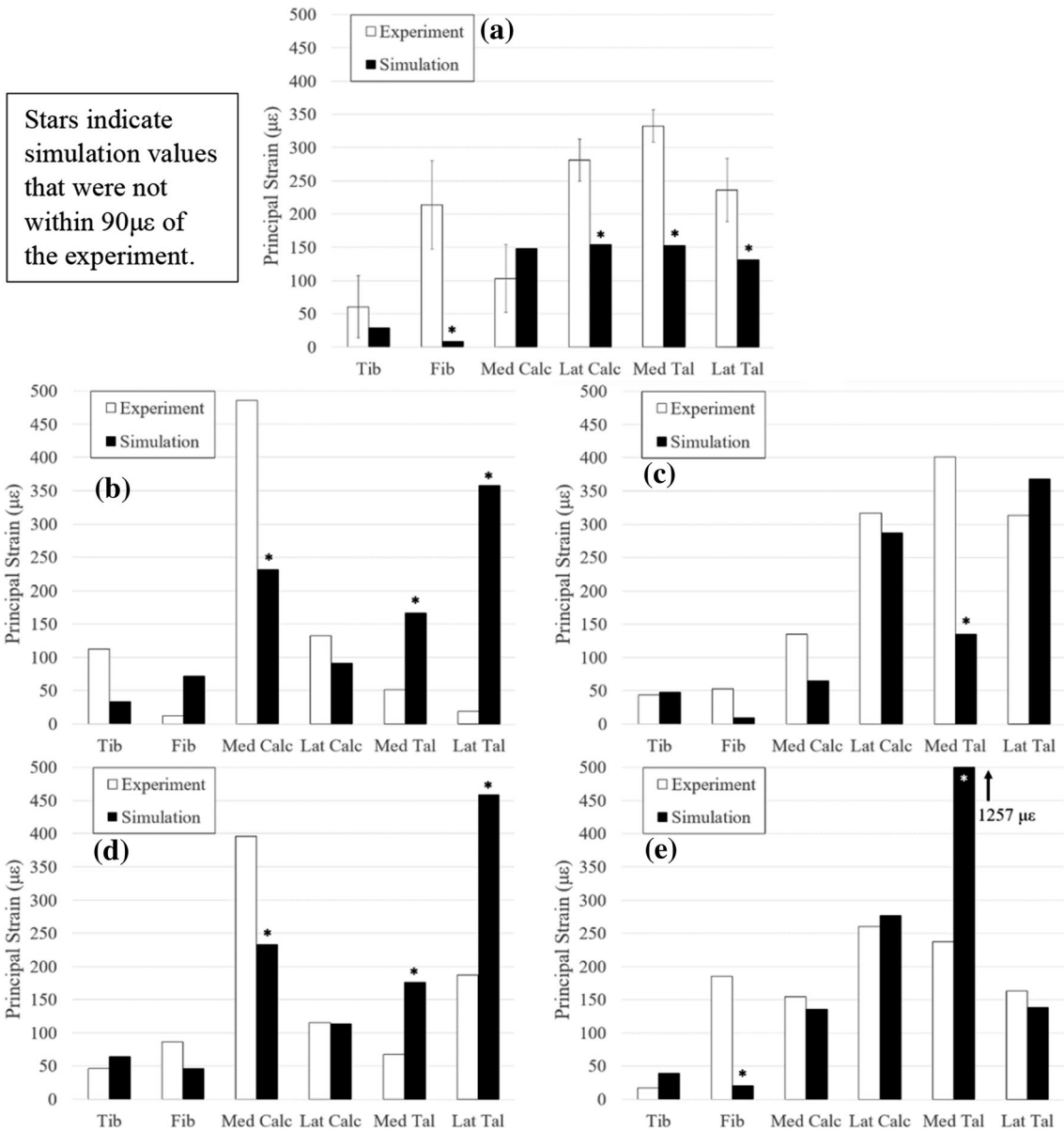
FIGURE 6. Comparison of experimental and simulated strains. The strains in the neutral (a), inversion–external rotation (b), eversion–external rotation (c), dorsiflexion-inversion (d) and plantarflexion (e) postures at 150 lbs of footplate compression are provided at the six strain gauge locations for both the FE simulation and the analogous experiment.[49] Tib, Fib, Med Calc, Lat Calc, Med Tal and Lat Tal represent the strain gauges located at the tibia, fibula, medial calcaneus, lateral calcaneus, medial talar neck and talar sulcus, respectively. Stars indicate simulation values that were not within 90 $\mu\varepsilon$ of the experiment.

cial attention was given to element quality, with several evaluation criteria used.

The simulated hindfoot bone rotations and displacements matched the experimental results very well at all postures. While the chosen limits were somewhat arbitrary, they are considered to constitute a fairly critical model evaluation when compared with the natural anatomic variation found within the population for talo-crural and talo-calcaneal joint motion brought about by isolated ankle rotations. For ankle rotations in plantarflexion/dorsiflexion, talar and calcaneal bone motion varied on average by over 300% relative to the mean, with similar figures observed for inversion/eversion and internal/external rotation.[47] The chosen threshold of 6° in the present study also constitutes a variation of talar and calcaneal bone motion of around 300% relative to the mean across all the postures tested.
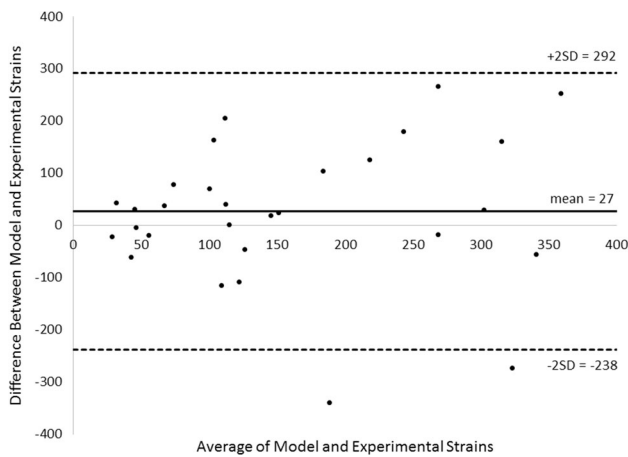
FIGURE 7. Bland–Altman plot of strains for all postures. Experimental and model strains from all gauge locations and all postures were combined into a Bland-Altman plot, with the exception of the medial talar gauge in plantarflexion (deemed to be erroneous). The differences between the model and experimental results showed small bias error (solid line) and moderate confidence interval (dashed line, indicating two standard deviations from the mean).
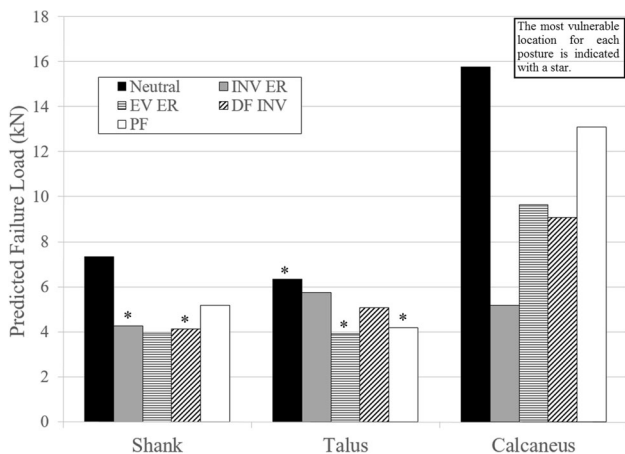

FIGURE 8. Predicted failure load in the shank and hindfoot for various postures. The footplate loads that would cause failure in the shank (fibula and tibia), talus and calcaneus were predicted based on the maximum strains measured in these bones at a footplate load of 150 lbs and the critical strain values for cortical and cancellous bone. The lowest failure load was predicted to be 3.9 kN, causing failure of the talus in the eversion–external rotation posture. INV-ER, EV-ER, PF and DF-INV denote the inversion–external rotation, eversion–external rotation, plantarflexion and dorsiflexon-inversion postures, respectively. The region where fracture was predicted to occur for each posture is identified with a star.

These results showed that biofidelic hindfoot bone positions can be produced in an FE model of the ankle by rotating a footplate attached to the plantar foot surface. However, the accuracy of these bone positions resulting from a footplate rotation cannot be guaranteed unless the center of rotation about each axis is known, and a sufficient number of ligaments and soft tissues are represented to control relative bone motion. This method of inducing ankle rotation has been used in previous lower limb FE studies[44,45] that contained detailed soft tissue models. However, the investigators were not able to calculate the exact centers of ankle rotation based on experimental CT data, potentially resulting in errors in individual bone positions and rotations.

Only the calcaneal displacement in eversion–external rotation exceeded the experimental result by the cut-off value, and this was most likely due to choosing the inferiorly-located calcaneal notch as the origin of the calcaneal coordinate system. In this posture, the calcaneus everted by nearly the threshold Euler angle (6°), potentially causing the calcaneal notch to be positioned too far laterally and overestimating the displacement. If the origin of the calcaneal coordinate system was located at a different location, for example at the superior aspect of the calcaneus, the excessive calcaneal eversion would not have had as much of a direct effect on this point. All minor bone positioning errors most likely stemmed from the absence of ligament pretension and cartilage in the model, imposing less restriction on bone rotation than in the natural foot and ankle. No known FE models of the foot and ankle have included ligament pretension due to a lack of experimental data available. Furthermore, the wrapping of ligaments around bones was also not simulated, and is beyond the scope of the current study. Cartilage is also typically neglected in injury predicting FE models of the lower limb. It is also worth noting that for several Euler angles, the model resulted in angles opposite to those observed in the experiment. This can be attributed primarily to the complex bone motions caused by the combined ankle rotations investigated in the present study. No Euler angle sign inversions were observed for the simplest ankle rotation that was produced: isolated plantarflexion. Once again, minor bone positioning errors due to the lack of ligament pretension in the model may have also played a role.

The tibial strains matched well for all postures, which supports the use of proximal tibia force–time responses for evaluating FE models. Fibular strains were underestimated in the neutral and plantarflexion postures, which may be attributed to neglecting cartilage in the model, causing a gap to be present between the talus and fibula, even at the maximum load. Fibular strains in these postures were therefore most likely caused only by ligament tension. A previous study examined the magnitude of load sharing between the tibia and fibula during various ankle postures,[15] and found that moving the ankle from inversion to eversion increased the percent of load borne by the fibula from approximately 3 to 16%. This corresponding increase in fibular load was not observed in
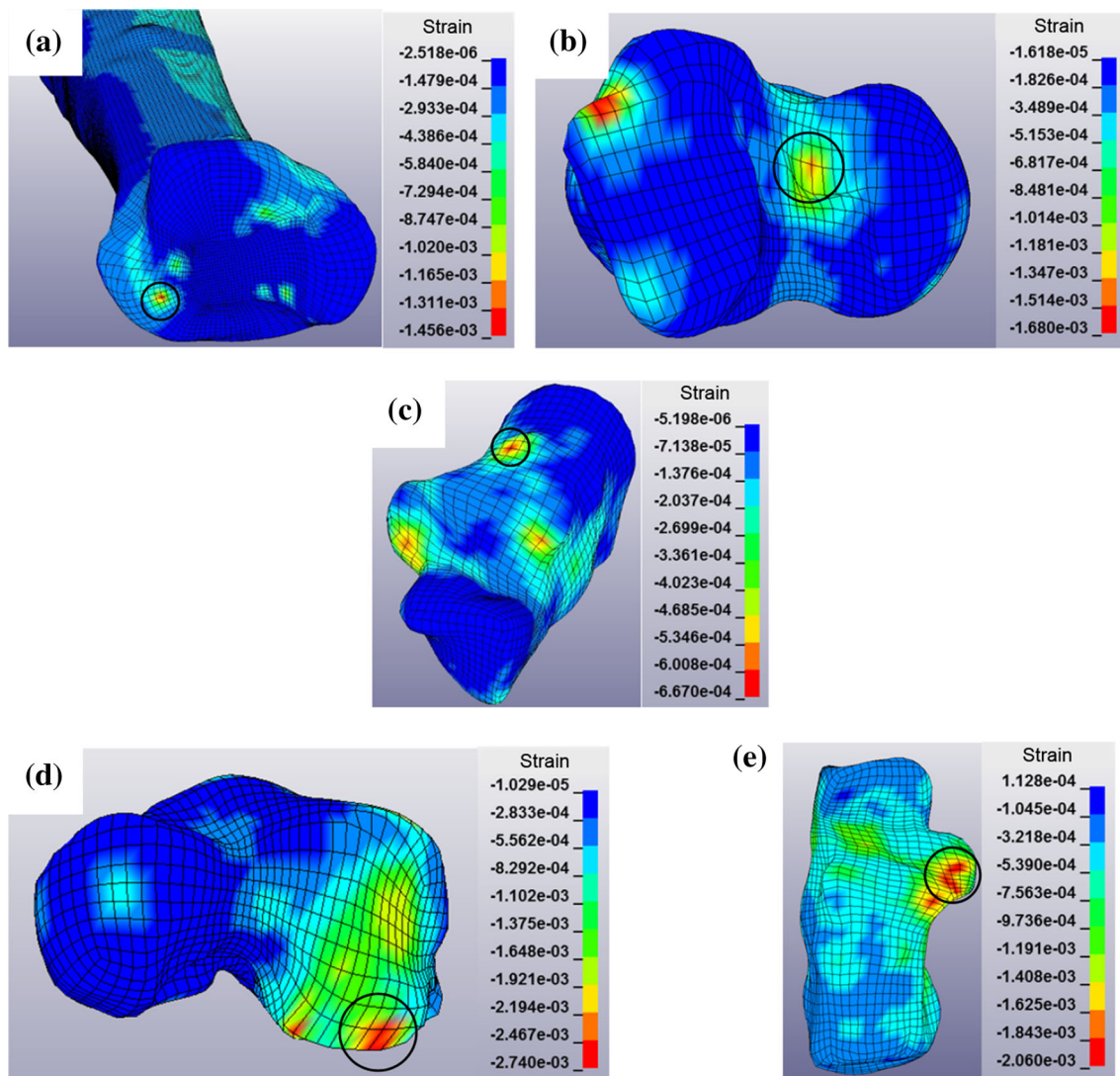
FIGURE 9. Lower leg model contour plots. Maximum principal strain contour plots in the neutral posture are provided for the shank (a), talus (b) and calcaneus (c). Contour plots are also provided for the talus in the eversion–external rotation posture (d), showing high strains at the lateral process, and at the calcaneus in the inversion–external rotation posture (e), showing high strains at the sustentaculum. Black circles indicate the locations of maximum strain. When present, locations of high strain adjacent to ligament connection nodes have been neglected due to point-loading effects. It should be noted that the color map range varies across each subfigure.

the present study (fibular load was in general negligible), and can also be attributed to the lack of cartilage and contact with the distal fibula. This would be an area of improvement in future iterations of the model.

Calcaneal strains generally matched well, but may be improved in the future through implementation of inhomogeneous properties,[51,57] possibly leading to more realistic strain fields through each bone, thus improving the surface strain match in all postures. No known injury-predicting models of the lower limb using hexahedral elements have implemented inhomogeneous properties.

The least successful strain agreement between the simulation and experiment was observed for the talar strains. While using homogenous and isotropic material properties likely contributed to this discrepancy, the main issue may be the gauge locations. In the current model, large strain gradients were observed at the two talar gauge locations (for example, a 690 $\mu\varepsilon$ difference between adjacent elements at the medial talus in plantarflexion). Due to these large gradients, minor bone positioning differences between the simulation and experiment may have resulted in substantial differences in load path, and thereby strain. The Bland–Altman plots also indicated the greatest errors in agreement at the talar locations. However, overall there was minimal bias error in the model – experimental evaluation, and the magnitude of the confi-

dence interval indicated on Fig. 7 was approximately three times that reported in a previous study on isolated ulnas.[35] Given the added complexity of the present full-limb model with numerous tissues and contacts, this was considered to be acceptable, and lends further support to the conclusion that component-level verification is an important part of future full limb models.

While hindfoot bone meshes in the current study were finer than those in previous lower limb FE models,[24,45] mesh size was investigated at an even finer density to assess whether the current mesh size was adequate. Overall the two meshes showed good agreement; however, strains in the fine mesh were larger in the tibia and smaller in the calcaneus. Thus, refining the model as such would have improved agreement with the experimental tibia strains, but reduced agreement at the calcaneus. This highlights the complexity in achieving agreement at a component level, but overall supports the use of the original mesh for this study. This method has its limitations, however, as it was not conducted at the altered postures, and only investigated one additional mesh density, with no indication of whether a coarser mesh could have been sufficient. Furthermore, if strain were compared at areas of lower curvature, with a more constant strain field, better agreement would most likely be achieved.

Most of the strain discrepancies in the present study are on the order of those observed in previous experimental studies due to anatomic variation within the population. In a previous study in which dynamic loading was applied to instrumented radii, principal strains were approximately 1000 $\mu\varepsilon$, with standard deviations of around 500 $\mu\varepsilon$.[2] A similar study by Staebler[52] reported standard deviations of 150–200 $\mu\varepsilon$ for average strains of 750 $\mu\varepsilon$. These results indicate that standard deviations of surface bone strain in the population are on the order of one half to one quarter of the average strains produced. In the current study, the average strains in the neutral posture were 205 $\mu\varepsilon$, meaning that the chosen threshold of 90 $\mu\varepsilon$ is within the previously observed range, making it a thorough and critical evaluation of the model.

The magnitude of the strain errors in the current study are consistent with those seen in previous injury-predicting bone models using strain gauges as a means of validation. For gauges on diaphysis/metaphysis locations, errors have been observed on the order of 25–45%,[4,37,54] but for epiphysis locations errors ranged up to 70%.[37] Due to the relative inhomogeneity of epiphyseal and hindfoot bone compared with diaphyseal bone,[51,57] it may be easier to achieve strain matching at the diaphysis of long bones using homogenous properties than at regions comprised primarily of cancellous bone, where the gauges were all located in the current study. The loads in the current model were also transmitted across multiple contact surfaces, which may have compounded any small errors.

The predicted fracture tolerance of the lower leg in the current study in a neutral posture was found to be 6.3 kN, which falls within the range of values reported by Yoganandan[58] (4.3–11.4 kN) and Funk[13] (3.7–8.3 kN). The predicted failure loads of all bones were always higher in the neutral posture than in all other tested postures, suggesting that the fracture tolerance of the lower leg may be overestimated in this posture. Since the majority of previous cadaveric and numerical studies predicting lower leg fracture tolerance have been conducted in a neutral posture,[24,58] more robust injury limits for this region accounting for variation in ankle position may be required. Limitations with the failure extrapolation in this study include the non-linearity of strains in the plastic region, and the exclusion of elements near ligament attachment nodes. However, the effect of these simplifications would be consistent across all simulations, making the relative comparisons (among bones and postures) still valid. The agreement with overall predicted failure loads also suggests that these effects may be relatively minor. As failure should occur in the bones of the ankle at several times the force of body weight, the application of axial loading of only 667 N (150 lbs) in both the experiment and simulation is also a limitation of this method of failure extrapolation.

Maximum strain locations were consistent with failure locations observed in previous experimental studies. The talus was predicted to have the lowest fracture tolerance in the neutral posture, and talar fractures were commonly observed in a study by Funk.[13] The maximum strain in the shank was at the distal tibia for all postures, which is consistent with commonly observed pilon fractures.[13,58]

The fracture tolerance of the calcaneus was lowest in inversion–external rotation at the sustentaculum, and fracture of this structure has been previously associated with inversion.[12] The lowest fracture tolerance of the talus was predicted to occur in eversion–external rotation at the lateral process of the talus, and these types of fractures are commonly attributed to excessive eversion.[16]

Other limitations associated with this study include the locations of the strain gauges, the lack of flesh in the model, and the number of specimens tested. With the exception of the maximum talar strain in the neutral and plantarflexion postures, which were located at the talar sulcus and the medial talar neck, respectively, the maximum strains were not generally in proximity to strain gauge positions. Therefore, the strains at these areas of particular vulnerability could not be validated, and

should be explored in the future. Another limitation was that strain directions were not investigated or validated in the present study, and should be examined further in the future, as it may have important implications for fracture development. Only plantar surface flesh was included, and this was considered to be acceptable as tissue compression only occurred at this location. Furthermore, flesh has been shown to only play a significant energy-absorbing role under dynamic impacts,[55] whereas only static loads were applied in the current study. Finally, the bone positions, rotations and strains were only compared for one specimen. If more specimens had been tested (generating biofidelity corridors), due to natural anatomical variation it is likely that the outcomes would have fallen well within the range found in the population.

This work has contributed to the understanding of the response and injury tolerance of the foot/ankle complex in non-neutral ankle postures. Several frequent limitations in FE modeling of the lower limb were investigated, such as mesh quality, the accuracy of hindfoot bone positions as posture is adjusted, and individual bones strain responses. The techniques employed in this work could be used in future studies to assess injury risk in other parts of the body or for developing new protective devices to reduce the occurrence of debilitating lower leg and ankle injuries.

CONFLICT OF INTEREST

None.

REFERENCES

[1]Bandak, F., R. Tannous, and T. Toridis. On the development of an osseo-ligamentous finite element model of the human ankle joint. *Int. J. Solids Struct.* 38:1681–1697, 2001.

[2]Burkhart, T. A., D. M. Andrews, and C. E. Dunning. Failure characteristics of the isolated distal radius in response to dynamic impact loading. *J. Orthop. Res.* 30:885–892, 2012.

[3]Burkhart, T. A., D. M. Andrews, and C. E. Dunning. Finite element modeling mesh quality, energy balance and validation methods: a review with recommendations associated with the modeling of bone tissue. *J. Biomech.* 46:1477–1488, 2013.

[4]Burkhart, T. A., C. E. Quenneville, C. E. Dunning, and D. M. Andrews. Development and validation of a distal radius finite element model to simulate impact loading indicative of a forward fall. *Proc. Inst. Mech. Eng. Part H* 228(3):258–271, 2014. doi:10.1177/0954411914522781.

[5]Burstein, A. H., D. T. Reilly, and M. Martens. Aging of bone tissue: mechanical properties. *J. Bone Jt. Surg.* 58:82–86, 1976.

[6]Castillo, R. C., E. J. MacKenzie, S. T. Wegener, and M. J. Bosse. Prevalence of chronic pain seven years following limb threatening lower extremity trauma. *Pain* 124:321–329, 2006.

[7]Cattaneo, P., M. Dalstra, and B. Melsen. The finite element method: a tool to study orthodontic tooth movement. *J. Dent. Res.* 84:428–433, 2005.

[8]Cheung, J. T.-M., K.-N. An, and M. Zhang. Consequences of partial and total plantar fascia release: a finite element study. *Foot Ankle Int.* 27:125–132, 2006.

[9]Crandall, J. R., D. Bose, J. Forman, C. Untaroiu, C. Arregui-Dalmases, C. G. Shaw, et al. Human surrogates for injury biomechanics research. *Clin. Anat.* 24:362–371, 2011.

[10]Dong, L., F. Zhu, X. Jin, M. Suresh, B. Jiang, G. Sevagan, et al. Blast effect on the lower extremities and its mitigation: a computational study. *J. Mech. Behav. Biomed. Mater.* 28:111–124, 2013.

[11]Erdemir, A., M. L. Viveiros, J. S. Ulbrecht, and P. R. Cavanagh. An inverse finite-element model of heel-pad indentation. *J. Biomech.* 39:1279–1286, 2006.

[12]Essex-Lopresti, P. The mechanism, reduction technique, and results in fractures of the os calcis. *Br. J. Surg.* 39:395–419, 1952.

[13]Funk, J. R., J. R. Crandall, L. J. Tourret, C. B. Macmahon, C. R. Bass, J. T. Patrie, et al. The axial injury tolerance of the human foot/ankle complex and the effect of Achilles tension. *J. Biomech. Eng.* 124:750–757, 2002.

[14]Funk, J., G. Hall, J. Crandall, and W. Pilkey. Linear and quasi-linear viscoelastic characterization of ankle ligaments. *J. Biomech. Eng.* 122:15–22, 2000.

[15]Funk, J. R., R. W. Rudd, J. R. Kerrigan, and J. R. Crandall. The line of action in the tibia during axial compression of the leg. *J. Biomech.* 40(10):2277–2282, 2007.

[16]Funk, J. R., S. C. Srinivasan, and J. R. Crandall. Snowboarder's talus fractures experimentally produced by eversion and dorsiflexion. *Am. J. Sports Med.* 31:921–928, 2003.

[17]Gabler, L. F., M. B. Panzer, and R. S. Salzar. High-rate mechanical properties of human heel pad for simulation of a blast loading condition. *Proceedings, IRCOBI Conference on the Biomechanics of Impact*, Berlin, Germany 2014.

[18]Golanó, P., J. Vega, P. A. J. de Leeuw, F. Malagelada, M. C. Manzanares, V. Götzens, et al. Anatomy of the ankle ligaments: a pictorial essay. *Knee Surg. Sports Traumatol. Arthrosc.* 18:557–569, 2010.

[19]Gray, H. Gray's Anatomy: With Original Illustrations by Henry Carter. London: Arcturus Publishing, 2009.

[20]Hofstede, D. J., M. J. Ritt, and K. E. Bos. Tarsal autografts for reconstruction of the scapholunate interosseous ligament: a biomechanical study. *J. Hand Surg.* 24:968–976, 1999.

[21]Hutton, W., and M. Dhanendran. A study of the distribution of load under the normal foot during walking. *Int. Orthop.* 3:153–157, 1979.

[22]Imai, K., I. Ohnishi, M. Bessho, and K. Nakamura. Nonlinear finite element model predicts vertebral bone strength and fracture site. *Spine* 31:1789–1794, 2006.

[23]Imhauser, C. W. The development and evaluation of a 3-dimensional, image-based, patient-specific, dynamic model of the hindfoot. PhD Dissertation, Drexel University, 2004.

[24]Iwamoto, M., K. Miki, and E. Tanaka. Ankle skeletal injury predictions using anisotropic inelastic constitutive model of cortical bone taking into account damage evolution. *Stapp Car Crash J.* 49:133, 2005.

[25]Kim, Y. S., H. H. Choi, Y. N. Cho, and Y. J. Park. Numerical investigations of interactions between the knee-thigh-hip complex with vehicle interior structures. *Stapp Car Crash J.* 49:85, 2005.

[26]Kitaoka, H. B., Z. P. Luo, E. S. Growney, L. J. Berglund, and K.-N. An. Material properties of the plantar aponeurosis. *Foot Ankle Int.* 15:557–560, 1994.

[27]Klopp, G., J. Crandall, G. Hall, W. Pilkey, S. Hurwitz, and S. Kuppa. Mechanisms of injury and injury criteria for the human foot and ankle in dynamic axial impacts to the foot. *Proceedings of the 1997 International IRCOBI Conference on the Biomechanics of Impact*, 1997.

[28]Kura, H., Z.-P. Luo, H. B. Kitaoka, W. P. Smutz, and K.-N. An. Mechanical behavior of the Lisfranc and dorsal cuneometatarsal ligaments: in vitro biomechanical study. *J. Orthop. Trauma* 15:107–110, 2001.

[29]Linde, F., I. Hvid, and B. Pongsoipetch. Energy absorptive properties of human trabecular bone specimens during axial compression. *J. Orthop. Res.* 7:432–439, 1989.

[30]MacKenzie, E. J., R. C. Castillo, A. S. Jones, M. J. Bosse, J. F. Kellam, A. N. Pollak, et al. Health-care costs associated with amputation or reconstruction of a limb-threatening injury. *J. Bone Jt. Surg.* 89:1685–1692, 2007.

[31]Manoli, A., P. Prasad, and R. S. Levine. Foot and ankle severity scale (FASS). *Foot Ankle Int.* 18:598–602, 1997.

[32]Mkandawire, C., W. Ledoux, B. Sangeorzan, and R. Ching. Hierarchical cluster analysis of area and length of foot and ankle ligaments. *Proceedings of the 25th Annual Meeting of the American Society of Biomechanics*, 2001, pp. 8–11.

[33]Mkandawire, C., W. R. Ledoux, B. J. Sangeorzan, and R. P. Ching. Foot and ankle ligament morphometry. *J. Rehabil. Res. Dev.* 42:809, 2005.

[34]Morris, A., P. Thomas, A. M. Taylor, and W. A. Wallace. Mechanisms of fractures in ankle and hind-foot injuries to front seat car occupants: an in-depth accident data analysis. *Proceedings of the 41st Stapp Car Crash Conference*, 13–14 November 1997, Orlando, FL (Sae Technical Paper 973328), 1997.

[35]Neuert, M. A. C., R. L. Austman, and C. E. Dunning. The comparison of density-elastic modulus equations for the distal ulna at multiple forearm positions: a finite element study. *Acta Bioeng. Biomech.* 15(3):37–43, 2013.

[36]Qian, S.-H., S.-R. Ge, and Q.-L. Wang. The frictional coefficient of bovine knee articular cartilage. *J. Bionic Eng.* 3:79–85, 2006.

[37]Quenneville, C. E., and C. E. Dunning. Development of a finite element model of the tibia for short-duration high-force axial impact loading. *Comput. Methods Biomech. Biomed. Eng.* 14:205–212, 2011.

[38]Ramasamy, A., S. D. Masouros, N. Newell, A. M. Hill, W. G. Proud, K. A. Brown, et al. In-vehicle extremity injuries from improvised explosive devices: current and future foci. *Philos. Trans. R. Soc. B* 366:160–170, 2011.

[39]Read, K. M., J. A. Kufera, P. C. Dischinger, T. J. Kerns, S. M. Ho, A. R. Burgess, et al. Life-altering outcomes after lower extremity injury sustained in motor vehicle crashes. *J. Trauma Acute Care Surg.* 57:815–823, 2004.

[40]Ritchie, R. O., M. J. Buehler, and P. Hansma. Plasticity and toughness in bone. *Phys. Today* 62:41–47, 2009.

[41]Rohen, J., C. Yokochi, and E. Lutjen-Drecoll. Color Atlas of Anatomy: Aphotographic Study of the Human Body. New York: Igaku-Shoin, 1992.

[42]Rudd, R. W. Updated analysis of lower extremity injury risk in frontal crashes in the United States. *21st International Technical Conference on the Enhanced Safety of Vehicles*, 2009.

[43]Sapuan, S., M. Osman, and Y. Nukman. State of the art of the concurrent engineering technique in the automotive industry. *J. Eng. Des.* 17:143–157, 2006.

[44]Shin, J., and C. D. Untaroiu. Biomechanical and Injury Response of Human Foot and Ankle Under Complex Loading. *J. Biomech. Eng.* 135:101008–101008, 2013.

[45]Shin, J., N. Yue, and C. D. Untaroiu. A finite element model of the foot and ankle for automotive impact applications. *Ann. Biomed. Eng.* 40:2519–2531, 2012.

[46]Shunmugasamy, V. C., N. Gupta, and P. G. Coelho. High strain rate response of rabbit femur bones. *J. Biomech.* 43:3044–3050, 2010.

[47]Siegler, S., J. Chen, and C. Schneck. The three-dimensional kinematics and flexibility characteristics of the human ankle and subtalar joints—part I: kinematics. *J. Biomech. Eng.* 110:364–373, 1988.

[48]Smith, P. N., and B. H. Ziran. Fractures of the talus. *Oper. Tech. Orthopaed.* 9(3):229–238, 1999.

[49]Smolen, C., and C. E. Quenneville. The effect of ankle posture on the load pathway through the hindfoot. *Proc. Inst. Mech. Eng. Part H* 230:1024–1035, 2016.

[50]Solan, M. C., C. T. Moorman, R. G. Miyamoto, L. E. Jasper, and S. M. Belkoff. Ligamentous restraints of the second tarsometatarsal joint: a biomechanical evaluation. *Foot Ankle Int.* 22:637–641, 2001.

[51]Souzanchi, M. F., P. Palacio-Mancheno, Y. A. Borisov, L. Cardoso, and S. C. Cowin. Microarchitecture and bone quality in the human calcaneus: local variations of fabric anisotropy. *J. Bone Miner. Res.* 27:2562–2572, 2012.

[52]Staebler, M. P., D. C. Moore, E. Akelman, A.-P. C. Weiss, P. D. Fadale, and J. J. Crisco. "The effect of wrist guards on bone strain in the distal forearm. *Am. J. Sports Med.* 27:500–506, 1999.

[53]Tannous, R. E., F. A. Bandak, T. G. Toridis, and R. H. Eppinger. A three-dimensional finite element model of the human ankle: development and preliminary application to axial impulsive loading. *SAE Technical Paper* 962427:0148–7191, 1996.

[54]Untaroiu, C., K. Darvish, J. Crandall, B. Deng, and W. Jenne-Tai. A finite element model of the lower limb for simulating pedestrian impacts. *Stapp Car Crash J.* 49:157, 2005.

[55]Untaroiu, C., K. Darvish, J. Crandall, B. Deng, and J.-T. Wang. Characterization of the lower limb soft tissues in pedestrian finite element models. *19th International technical conference on the Enhanced Safety of Vehicles*, 2005, pp. 124–131.

[56]Valle, L., and M. Ray. Development and Validation of a 50th Percentile Male Human Femur: Attachment A. Worcester, MA: National Highway Traffic Safety Administration, Worcester Polytechnic Institute, 2005.

[57]von Meyer, G. H. The classic: the architecture of the trabecular bone (tenth contribution on the mechanics of the human skeletal framework). *Clin. Orthop. Relat. Res.* 469:3079–3084, 2011.

[58]Yoganandan, N., F. A. Pintar, M. Boynton, P. Begeman, P. Prasad, S. M. Kuppa, *et al.* Dynamic axial tolerance of the human foot-ankle complex. SAE Technical Paper 962426, 1996.